

Temperature Evolution of Methylammonium Trihalide Vibrations at the Atomic Scale

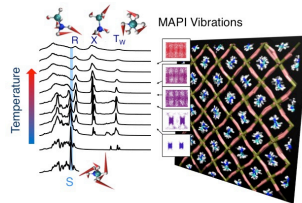
A. Mattoni,* A. Filippetti, M.I. Saba, C. Caddeo, and P. Delugas

Istituto Officina dei Materiali, CNR-IOM SLACS Cagliari, 09042 Monserrato (CA)

E-mail: mattoni@iom.cnr.it

Abstract

The temperature evolution of vibrations of $\text{CH}_3\text{NH}_3\text{PbI}_3$ (MAPI) is studied by combining first-principles and classical molecular dynamics and compared to available experimental data. The work has a fundamental character showing that it is possible to reproduce the key features of the vibrational spectrum by the simple physical quantities included in the classical model, namely the ionic-dispersive hybrid interactions and the mass difference between organic and inorganic components. The dynamics reveals a sizable temperature evolution of the MAPI spectrum along with the orthorhombic-to-tetragonal-to-cubic transformation and a strong dependence on molecular confinement and order. The thermally-induced weakening of the H-I interactions and the anharmonic mixing of modes give two vibrational peaks at $200\text{-}250\text{ cm}^{-1}$ that are not present at zero temperature and are expected to have detectable infrared activity. The infrared inactive vibrational peak at $\sim 140\text{ cm}^{-1}$ due to molecular spinning disappears abruptly at the orthorhombic-to-tetragonal transition and forms a broad molecular band red-shifting progressively with temperature. This trend is correlated to the reduced confinement of the rotating cations due to thermal expansion of the lattice.



The discovery of methylammonium lead tri-halide (MAPI)¹⁻³ as one of the best performing solution processable organic-inorganic materials for photovoltaics has attracted great interest on the study of hybrid perovskites and their fundamental properties.⁴⁻⁹ The origin of the excellent photovoltaic performances of MAPI has been searched in its optoelectronic properties and in the nature of its excitations¹⁰⁻¹⁴. The current understanding is that the electronic levels of the organic MA cations are optically inactive and separated in energy from the gap that is instead formed by large delocalized Pb,I orbitals;¹⁵ the result is a material with hybrid composition that behaves as an inorganic PI-based semiconductor for what concerns electron-hole excitations, optoelectronic and transport properties.^{14,16}

The role of organic cations and the hybrid nature of MAPI become manifest when considering its dynamical properties and the effect of temperature. It is well established that the changes in molecular orientation induce distortions in the Pb-I orbitals overlap^{5,9,15} and indirectly affect the electronic gap, the effective mass tensor, the dielectric function and absorption coefficients.¹⁵ The interaction of the MA cations with the inorganic lattice has an impact on the thermal conductivity,¹⁷ the electron-phonon coupling, and transport,¹⁸ recombination¹⁹ and luminescence properties.^{13,20} Also the ferroelectric response of the material depends on the ordering of cation dipoles²¹ and it is suppressed, even at low temperatures, because of the molecular entropy that is peculiar of the hybrid nature of the material.²²

Temperature is the key parameter that tunes the organic-inorganic interactions and the MA dynamics.²³⁻²⁷ Recently, molecular dynamics simulations²⁸ have shown that at low temperature the molecules are constrained in the orthorhombic crystal and harmonically vibrate around local equilibrium configurations; as the temperature increases the organic cations pro-

gressively explore a larger set of configurations and, beyond the orthorhombic-to-tetragonal transition ($T=160$ K), the temperature gives rise to a complex anharmonic dynamics with fast reorientations.

Phonons and vibrations have great relevance in this context. Vibrational frequencies of MAPI have been studied by infrared (IR),^{29–31} Raman spectroscopy,^{32,33} nuclear magnetic resonance²³ and by neutron spectroscopy.^{24,25} From the theoretical point of view, first principles methods have been applied.^{32,34,35} The harmonic approximation was used to calculate the vibrational density of states (VDOS) and infrared (IR) spectra of the tetragonal, orthorhombic^{32,35} and cubic phases.³⁴ Ab initio molecular dynamics were used by Mosconi et al.³⁰ to calculate the IR spectra of MAPI, though a few temperatures have been studied because of the computational cost of first-principles methods.³⁰ Important information can be extracted from the temperature dependence of the vibrational spectra; for example, the evolution of the molecular peaks at $900\text{--}1000\text{ cm}^{-1}$ gives insight into the orthorhombic-tetragonal phase transition and the MA relaxation times.²⁹ The Raman and IR temperature dependent bands observed in the tetragonal phase at $200\text{--}300\text{ cm}^{-1}$ could provide information on molecular order³² or degradation phenomena.^{33,35,36} A comprehensive theoretical study of the temperature evolution of MAPI vibrations beyond the harmonic approximations and beyond the limit of ab initio approaches is necessary to clarify the atomic scale origin of the vibrational peaks at finite temperatures.

In this Letter, we combine density functional calculations (DFT) and classical molecular dynamics (MD) to study the temperature dependence of MAPI vibrations on a dense grid of values and we correlate the vibrations with the thermodynamic evolution. The work has a fundamental character showing that it is possible to qualitatively reproduce the vibrational spectrum by the simple physical quantities included in the classical model. By MD we are able to analyze relatively large systems without applying any constraint on the crystal structure and its lattice parameters that are controlled by the finite-temperature dynamics. We make use of the MYP potential, recently developed by Mattoni et al.²⁸ that was

proved to reproduce the cation reorientations with temperature. We show that the ionic nature of the organic-inorganic interactions and the mass difference between organic and inorganic ions are able to explain the qualitative structure of phonon dispersion, the progressive separation in frequency between the organic-inorganic modes and the evolution of the vibrational peaks with temperature. By projecting the VDOS on the different atomic components we characterize the dynamical modes at finite temperature and correlate them to the orthogonal-to-tetragonal phase transition. In particular, we unveil the presence of two twisting modes at 200-300 cm^{-1} which, while vanishingly small at zero T, appear at $T=50$ K. Those are precursive signals of the internal decoupling between MA and PbI sublattices, which is then fully accomplished at the ortho-tetra transition temperature. The theoretical results are discussed against available experimental data.

In the hybrid MAPI crystal, the normal frequencies of the MA cations are affected by the electrostatic potential of the embedding inorganic PI sublattice. This is shown in Figure 1 where the vibrational modes of the isolated MA molecule (column c) are compared with the total VDOS of the orthorhombic MAPI crystal (column d). Normal frequencies and modes were obtained by the static method (Supporting Information, SI) consisting in the diagonalization of the dynamical matrix calculated through finite-differences under harmonic approximation at zero temperature by the QUANTUM ESPRESSO code.³⁷ The vibrational spectrum of the isolated MA molecule has six roto-translations (R-T) at zero frequency. The other internal modes consist of singlets or doublets corresponding to the C_{3v} molecular symmetry (SI, Figure S3). The lowest one at 290 cm^{-1} is the twisting T_w around C-N axis (see inset); two breathings (i.e. rocking) are found at 879 cm^{-1} (B_1) and one C-N stretching mode at 980 cm^{-1} (S_t). The modes at higher frequencies are more localized, the highest ones above 3000 cm^{-1} associated to the rocking and bending of the NH_3 group. The full analysis of the DFT and MYP methylammonium spectra can be found in the SI, Figures S3 and S5) and is consistent with the data reported in literature.^{32,34,35}

The MAPI spectrum of the orthorhombic crystal calculated with the same static method

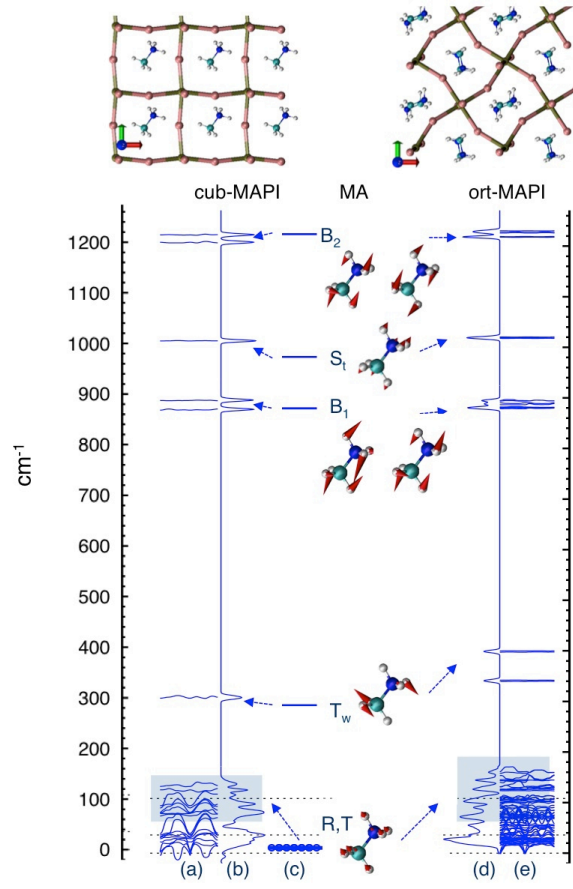


Figure 1: Vibrational spectrum in the isolated MA cation (middle column, c) compared to cubic (column b) and orthorhombic (column d) MAPI crystals. The corresponding phonon dispersion curves are reported (columns a,e for cubic and orthorhombic, respectively).

is reported in panel d of Figure 1. It can be neatly separated in two regions: below 200 cm^{-1} (shadowed regions) the direct coupling of MA and PI sublattice gives rise to mixed modes spurring from the relative motions of molecules and octahedra^{34,35} (formed by PI modes and 6 roto-translations per molecule). Above this threshold, only flat molecular modes appear, eventually energy-shifted or degeneracy-broken with respect to the single-molecule values by the effective action of the surrounding PbI_3 potential.

For example, the free molecule twisting mode T_w at 290 cm^{-1} splits into two doublets blue shifted at 350 and 400 cm^{-1} . At higher frequencies, as the modes become more localized the effect of the crystal and the blue shift is smaller (for the B_1 the blue shift is as small as $\sim 20\text{ cm}^{-1}$).

In column e, we further report the phonon dispersion of the orthorhombic crystal (that is extensively discussed below, see Figure 2). The absence of dispersion confirms the localization of molecular levels above 300 cm^{-1} . Conversely, a sizable dispersion of molecular levels is observed in the $100\text{-}200\text{ cm}^{-1}$ vibrational band.

Notice that the phonon spectrum at $T=0\text{ K}$ refers to a single, specific molecular configuration, while it was shown that the low- T phase of this material is characterized by a plethora of metastable structures with different MA orientations.¹⁵ The MAPI spectrum, and in particular, the molecular band below 200 cm^{-1} slightly changes depending on the crystal structure and molecular order. For example, the cubic phase (panels a, b) exhibits a shrunk molecular band because of the higher cubic symmetry. Furthermore, the spectra of orthorhombic MAPI with alternative MA orientations (reported in SI, Figure S6) depend on the actual configuration though the main features are unaltered. In this sense, our T -dependent MD simulation (see below) is a much more adequate treatment of the atomic vibrations than $T=0$ DFT results. In particular, MD is required to study the high- T phases of MAPI (tetragonal and cubic) and it is free of imaginary frequencies (i.e. instabilities) occurring for example in the study of the cubic phase at zero temperature. Furthermore, MD is able to include anharmonic effects on the position and the height of the vibrational peaks

(e.g. phonon lifetime) at finite temperature (SI, Figure S8).

The tetragonal crystal is the most relevant for applications and will be analyzed by MD in the T- range 180-300 K. Here we focus on the DFT static analysis of the orthorhombic phase (Figure 2) since it is the equilibrium MAPI crystal at T=0 K; we report for completeness the static analysis of tetragonal (by MYP) and cubic phase (by both MYP and ab initio) in the SI, Figure S8. Different colors are used to highlight the contribution of organic and inorganic components in Figure 2. A color palette, continuously varying from yellow (organic) to steel-blue (inorganic) is used to represent the calculated MA character (see SI, static calculation of phonons). The phonon calculation in the orthorhombic phase is quite computationally demanding and Gamma point is typically used.^{30,32,34,35} Here, we make use of a real space finite difference approach making it possible to calculate large 2x2x2 systems of 384 atoms (see SI, Figure S1). Notably, all the imaginary modes are removed (see SI, Figure S4 for a comparison with the cubic phase).

The phonon analysis confirms that internal modes at 340 and 390 cm^{-1} (T_w) already attributed to twisting modes have in fact a strong molecular character (yellow) and vanishingly small dispersion. The calculated eigenvectors (see Figure 2) confirm the twisting of the molecules.

The vibrational band at low frequencies consists as expected of 72 modes (18 modes per four formula units, consisting of 6 MA roto-translations plus 12 PbI_3 atomic displacements). It can be separated into three regions: an inorganic band at low frequencies 0-70 cm^{-1} ; a mixed organic-inorganic region at 70-120 cm^{-1} ; a molecular band at 120-180 cm^{-1} . It is possible to roughly identify six molecular peaks spanning over the mixed and molecular bands at frequencies (in cm^{-1}): 80 (R_C), 105 (T), 125 (R_N), 145 (S), 165 (R). The corresponding molecular modes (calculated at the Γ point) are reported in Figure 2. The letters R,S,T, T_w refer to rotation (i.e. libration), spinning, translations and twisting modes, respectively (light blue/dark-blue is used for modes involving atoms of the methyl/ammonium groups, respectively; black is used for translations). Furthermore, R_C and R_N are used for rotational

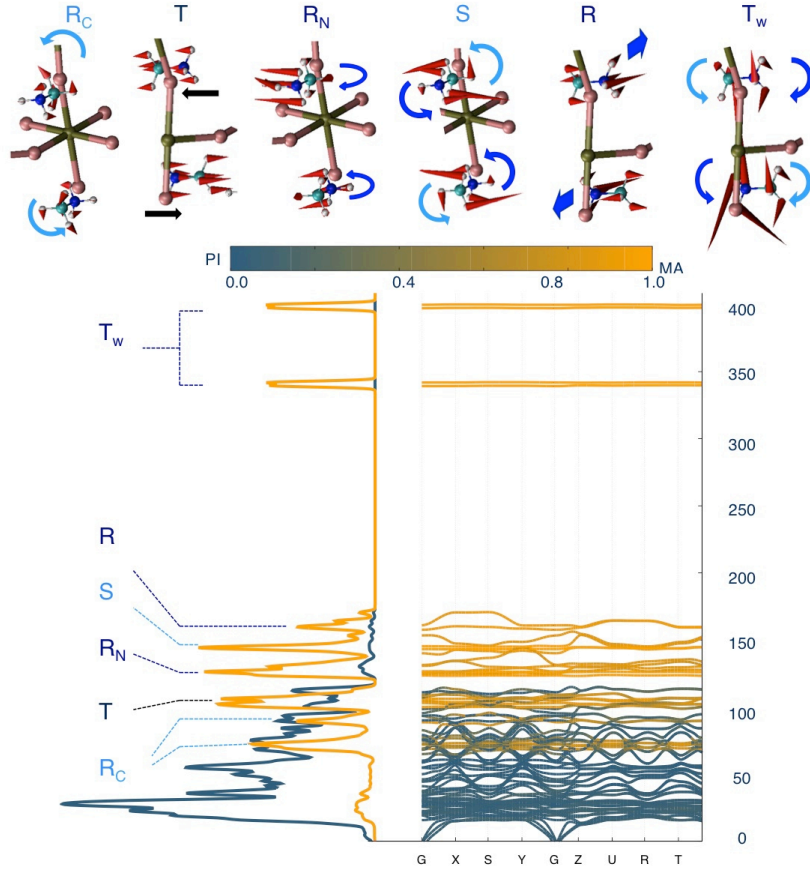


Figure 2: Vibrational density of states (left) and phonon dispersion (right) of the orthorhombic MAPI crystal calculated by DFT; colors indicate the projection on the organic/inorganic components (yellow/steel blue, respectively). Molecular peaks (orange) are labeled by letters R_C , T , R_N , S , T_w , R corresponding to rotations (R_C and R_N refers to larger displacements on methyl or ammonium, respectively), translations, spinning, twisting; the corresponding representative modes are reported in the top insets where only two molecules of the unit cell were represented for clarity; red cones are the atomic displacements and arrows³⁸ represent the type of molecular mode.

modes with larger displacements on the CH_3 and NH_3 groups, respectively. The higher frequency of R_N modes is consistent with the stronger I-NH_3 interactions. The peak at 140 cm^{-1} (blue) corresponds to the spinning of the methylammonium cations around their CN axis (S). This simple classification is still valid for phonons of tetragonal (SI, Figure S8) or orthorhombic configurations with different molecular orientations (SI, Figure S7) and adopted here instead of more detailed symmetry group analysis.³⁵

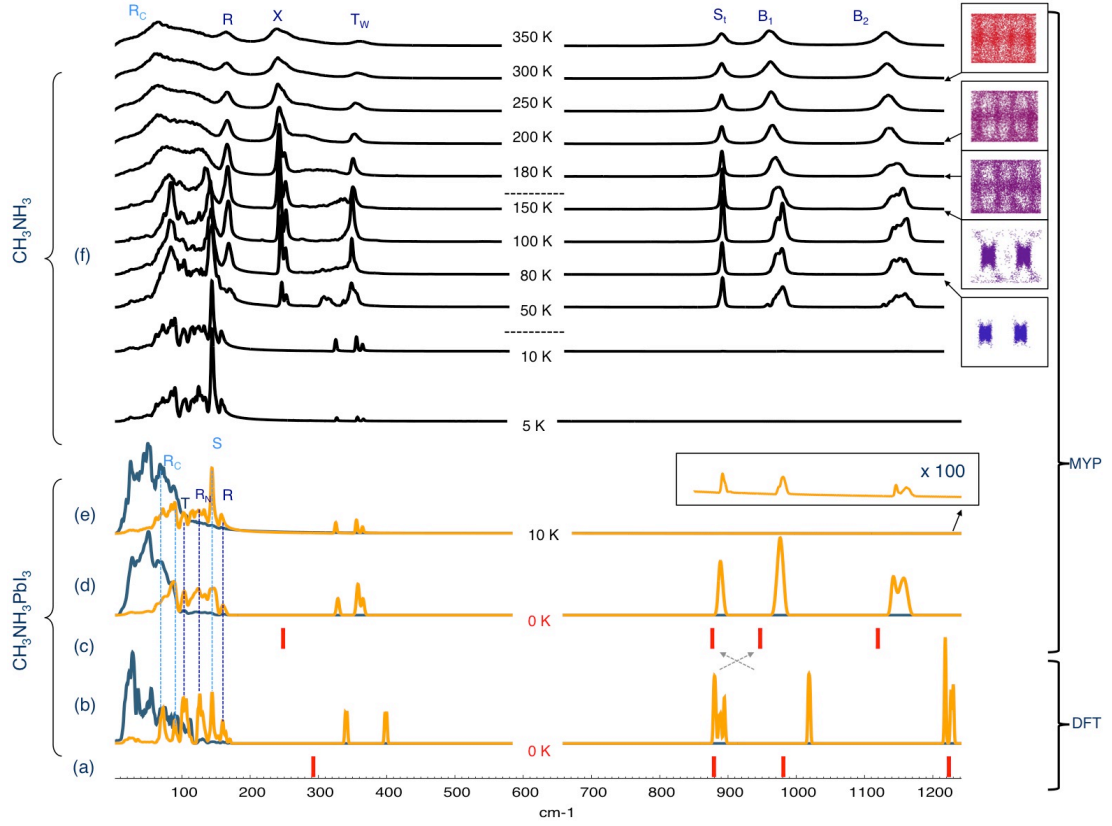


Figure 3: Panels f: temperature evolution of the MA-projected vibrational density of states of MAPI obtained by molecular dynamics; it is also reported the reference static spectra at $T=0 \text{ K}$ of MAPI (panel b and d) and isolated MA (panel a and c) obtained by DFT and by MYP, respectively; panel e is the dynamic MD result at $T=10 \text{ K}$ (orange and blue are MA and PI projections, respectively).

It is also remarkable that the vibrational structure does not depend strongly on the details of the MAPI electronic structure. In fact vibrational spectrum can be reproduced qualitatively by the classical ionic MYP potential (see panel c and d of Figure 3). Atomic

forces were calculated by the DL_POLY code³⁹ (SI, atomic forces calculation). The MYP model includes electrostatic and dispersive interactions in the spirit of models successfully applied to study polymer-oxide^{40,41} and molecule-oxide^{42,43} hybrid systems and it reproduces qualitatively both the spectrum of the isolated MA (panel c) and the MAPI phonon dispersions (panel d) and their organic-inorganic projections, with continuous vibrational band at 0-200 cm^{-1} followed by discrete molecular modes up to beyond 3000 cm^{-1} . Similarly to the DFT it is also observed the tendency of the MA normal frequencies to blue shift within MAPI.

The quantitative agreement with DFT (panel b and d) has been obtained by rescaling the width of the MYP band by a factor ~ 1.3 (SI, Figure S7). The agreement is remarkable, considering that it includes parameters not directly optimized on the vibrational properties. Moreover the MYP consists of classical 2-body electrostatic forces for the description of hybrid and PI interactions.²⁸ This also indicates that the vibrational features of MAPI are mostly related to the ionic character (nominal charges) and the mass difference between light organic and heavy inorganic components.

Having validated the MYP model, we apply it to study the evolution of vibrational properties with temperature (see Figure 3). This is obtained by calculating the velocity autocorrelation function during molecular dynamics (see SI, finite temperature dynamical calculations). The reduced computational cost of the classical simulations makes large systems and long annealings affordable in a broad range of temperatures (0-350 K) without applying any constraint on the crystal structures and volumes, only determined by the simulation temperature.

The result at 10 K is reported in panel e, Figure 3. Similarly to the static method it is possible to disentangle in the VDOS the PI and MA contributions, the latter reported as a function of temperature in panels f. As expected, at such low temperatures, the dynamic methods (e) is close to the static harmonic approximation (d). There are slight differences: the S peak at about 140 cm^{-1} is higher due to the coalescence of the closest peaks; the

molecular modes above $\omega > 400 \text{ cm}^{-1}$ are not activated at such low temperatures (an inset with magnification is reported). In the range 10-50 K the R peak evolves towards higher frequencies and the internal MA modes at $\omega > 800 \text{ cm}^{-1}$ become visible. Notably, at T=50 K a peak appears at 250 cm^{-1} (X) not present at all in the orthorhombic spectrum (d). From 50 to 150 K, while the crystal remains orthorhombic, a progressive decrease of S together with an increase of R, X and T_w peaks is found. In particular, the T_w doublets that are separated at T=50 K evolve into a single structure as T approaches 180 K.

A sudden change in the VDOS is found from 150 K to 180 K, associated to the orthorhombic-to-tetragonal thermodynamic transition. The rotational maps of MA cations are reported for reference and show that MA cations modify dramatically their trajectories beyond the transition.²⁸ Below 160 K in the orthorhombic phase the molecules are strongly constrained in presence of the PI lattice. At T>180 K, the PI lattice expands in the tetragonal phase and the molecules undergo fast reorientations corresponding to a quasi-uniform distribution of molecular directions in the spherical map. At the transition, the S peak disappears and gives rise to a broad shoulder involving T and R_N ; this evolution is consistent with the spinning character of the S mode that is lost as soon as the molecules are not constrained and can change directions in the expanded tetragonal lattice. Conversely, the R_C peak survives after the transition but it progressively redshifts with temperature. This is consistent with the rotational character of R_C mode and the reduced confinement of the molecules with the thermal expansion.

To further clarify the physical interpretation of the peaks and their evolution, we report in Figure 4 the cases T=10 K, 50 K and 300 K corresponding to the three possible regimes described above. In addition to the usual MA projections we also report the projections on PI, H, C and N. Light-blue refers to atoms of the methyl group (H_C , or C); dark-blue to the ammonium group (H_N , N). Also the the total VDOS (red) and PI projections are given for comparison.

By Fourier transforming the velocities we are also able to analyze the modes during the

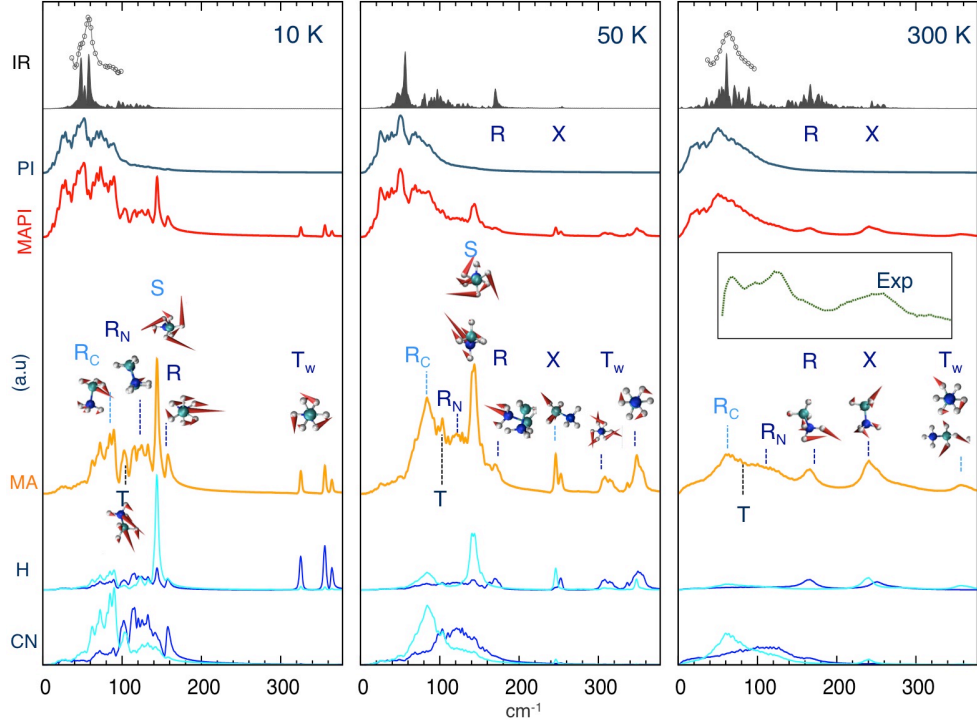


Figure 4: Projected density of states on PI (inorganic), MAPI (total), MA(organic), and H,C,N atoms; light blue refers to H,C of CH_3 ; dark blue refers to H,N of NH_3 ; top panels report the calculated IR spectra (lines) calculated with fixed charges (see SI, finite temperature dynamical calculation) and experimental spectroscopic data⁴⁴ (circles); inset of right panel: Raman measurements of the tetragonal phase.³²

dynamics and we report the relevant ones as stick&balls insets at the corresponding peaks; one or two molecules have been selected in each case from the 256 molecules (see SI, Figure S2). At $T=10$ K the analysis agrees with the zero temperature harmonic approximation (left panel of Figure 4). By considering the H and CN projections, and moving from low to high frequency, it is found that: the R_C peak has C character, the translations T have a mixed CN character, the S spinning mode projects mainly on hydrogens with predominance of methyl group, the R peak has a roto-translation character with large N projection (see inset), the twisting T_w close to 400 cm⁻¹ involves hydrogens, with large contributions from the ammonium.

The same qualitative decomposition is found at $T=50$ K and $T=300$ K, as shown by the fact that the light-blue curves are always shifted to lower frequencies. In particular at $T=50$ K (middle panel) the analysis clarifies that: the S reduction and broadening are due to the mixing with modes at different frequencies (see the two molecules in the inset at S peak); the blue shift of the R mode corresponds to a larger N projection and a reduced spinning character; the T_w twisting modes start mixing with breathings (see the two peaks above 350 cm⁻¹). Important, the new X mode at 250 cm⁻¹ (corresponding to the twisting of the free MA and consistent with a peak in the cubic phase of Figure 1) is not a pure twist but mixed with breathings on H_C and H_N . The appearance of the X mode can be explained in terms of thermally activated weakening of H-I interactions; at $T<10$ K the H-I interaction gives an additional torque to the molecule twist that blue shifts it from 300 cm⁻¹ of the isolated cation to 350-400 cm⁻¹ (left panel of Figure 4); at higher temperatures the internal vibrations overcome the H-I constraints and the peak at 250 cm⁻¹ appears. The fact that the mode is mixed with breathings can be inferred from the larger C projections (at variance with T_w). The X mode persists at 300 K and becomes a rocking mode (see inset).

The above evolution concerns the phonons and vibrational density of states. For completeness, we calculate the infrared spectrum (top panel) by using fixed atomic charges (see SI, finite temperature dynamical calculations). The IR spectrum follows the evolution of

the vibrational spectra, however because of its A_2 symmetry, the S mode is inactive, consistent with previous findings.³⁵ Conversely, the R mode is expected to have optical activity with a contribution around 200 cm^{-1} . The temperature evolution of the MAPI vibrations in the low frequency range (below 100 cm^{-1}) has been recently characterized by Terahertz Time-Domain Spectroscopy.⁴⁴ The spectrum of MAPI at low temperature shows a peak at 40-60 cm^{-1} in agreement with previous experimental findings^{30,32,34,35} that is reproduced by our calculations (see top panels); at increasing temperature the peak slightly blue-shifts forming at 300 K a shoulder above 60-70 cm^{-1} (symbols of top right panel⁴⁴). This trend is reproduced by the simulated phonons and IR spectrum (see also SI, Figure S9). Concerning the vibrational spectra at higher frequencies ($\omega > 100 \text{ cm}^{-1}$), the calculated R and X molecular peaks can be compared with similar features in Raman³² (inset in right panel of Figure 4) and IR measurements.³⁰ However, we notice that such features are also affected by degradation during measurements³³ making difficult a conclusive attribution based on the experimental data available in literature.

In conclusion, the present analysis clarifies the phonons and the temperature evolution of MAPI vibrations and makes it possible to attribute the molecular modes by including anharmonic effects associated to the finite temperature. It is found a clear correlation of the low energy S peak at around 140 cm^{-1} with the orthorhombic-to-tetragonal transition, while mixed twisting and breathings modes in the 200-300 cm^{-1} can be attributed the weaker H-I bonding and show sizable evolution even at lower temperature in the orthorhombic phase.

Acknowledgement

We acknowledge financial support by Istituto Italiano di Tecnologia under Project CompuNet, by Regione Autonoma della Sardegna (CRP-24978 and CRP-18013), by Fondazione Banco di Sardegna (Project 7454, 5794). We acknowledge computational funding by CINECA, Italy through ISCRA Projects VIPER and THESTA.

Supporting Information Available

Methodological details on static phonons, atomic forces and finite temperature dynamical calculations; ab initio MA spectrum; ab initio cubic-MAPI phonons and cubic-to-orthorhombic instabilities; comparison between MYP and DFT; MYP rescaling and effects of molecular order on the orthorhombic MAPI phonons; cubic-, tetragonal- and orthorhombic-MAPI phonons by MYP: static versus dynamic results; comparison with experiments.

References

- (1) Kojima, A.; Teshima, K.; Shirai, Y.; Miyasaka, T. Organometal halide perovskites as visible-light sensitizers for photovoltaic cells. *J. Am. Chem. Soc.* **2009**, *131*, 6050–1.
- (2) Lee, M. M.; Teuscher, J.; Miyasaka, T.; Murakami, T. N.; Snaith, H. J. Efficient hybrid solar cells based on meso-superstructured organometal halide perovskites. *Science* **2012**, *338*, 643–7.
- (3) Burschka, J.; Pellet, N.; Moon, S.-J.; Humphry-Baker, R.; Gao, P.; Nazeeruddin, M. K.; Grätzel, M. Sequential deposition as a route to high-performance perovskite-sensitized solar cells. *Nature* **2013**, *499*, 316–9.
- (4) Yin, W.-J.; Yang, J.-H.; Kang, J.; Yan, Y.; Wei, S.-H. Halide perovskite materials for solar cells: a theoretical review. *J. Mater. Chem. A* **2014**,
- (5) Mosconi, E.; Amat, A.; Nazeeruddin, M. K.; Grätzel, M.; De Angelis, F. First-principles modeling of mixed halide organometal perovskites for photovoltaic applications. *J. Phys. Chem. C* **2013**, *117*, 13902–13913.
- (6) Giorgi, G.; Yamashita, K. Organic-Inorganic halide perovskites: an ambipolar class of materials with enhanced photovoltaic performances. *J. Mater. Chem. A* **2014**, *3*, 8981–8991.

- (7) Even, J.; Pedesseau, L.; Jancu, J.-M.; Katan, C. Importance of spin-orbit coupling in hybrid organic/inorganic perovskites for photovoltaic applications. *J. Phys. Chem. Lett.* **2013**, *4*, 2999–3005.
- (8) Stroppa, A.; Di Sante, D.; Barone, P.; Bokdam, M.; Kresse, G.; Franchini, C.; Whangbo, M.-H.; Picozzi, S. Tunable ferroelectric polarization and its interplay with spin-orbit coupling in tin iodide perovskites. *Nat. Commun.* **2014**, *5*, 5900.
- (9) Filip, M. R.; Eperon, G. E.; Snaith, H. J.; Giustino, F. Steric engineering of metal-halide perovskites with tunable optical band gaps. *Nat. Commun.* **2014**, *5*, 5757.
- (10) Stranks, S. D.; Eperon, G. E.; Grancini, G.; Menelaou, C.; Alcocer, M. J. P.; Leijtens, T.; Herz, L. M.; Petrozza, A.; Snaith, H. J. Electron-hole diffusion lengths exceeding 1 micrometer in an organometal trihalide perovskite absorber. *Science* **2013**, *342*, 341–4.
- (11) Saba, M.; Cadelano, M.; Marongiu, D.; Chen, F.; Sarritzu, V.; Sestu, N.; Figus, C.; Aresti, M.; Piras, R.; Geddo Lehmann, A. et al. Correlated electron-hole plasma in organometal perovskites. *Nat. Commun.* **2014**, *5*, 5049.
- (12) D’Innocenzo, V.; Grancini, G.; Alcocer, M. J. P.; Kandada, A. R. S.; Stranks, S. D.; Lee, M. M.; Lanzani, G.; Snaith, H. J.; Petrozza, A. Excitons versus free charges in organo-lead tri-halide perovskites. *Nat. Commun.* **2014**, *5*, 3586.
- (13) Grancini, G.; Srimath Kandada, A. R.; Frost, J. M.; Barker, A. J.; De Bastiani, M.; Gandini, M.; Marras, S.; Lanzani, G.; Walsh, A.; Petrozza, A. Role of microstructure in the electron-hole interaction of hybrid lead halide perovskites. *Nat. Photonics* **2015**, *9*, 1–15.
- (14) Sestu, N.; Cadelano, M.; Sarritzu, V.; Chen, F.; Marongiu, D.; Piras, R.; Mainas, M.; Quochi, F.; Saba, M.; Mura, A. et al. Absorption F-sum rule for the exciton binding

- energy in methylammonium lead halide perovskites. *J. Phys. Chem. Lett.* **2015**, 4566–4572.
- (15) Filippetti, A.; Mattoni, A. Hybrid perovskites for photovoltaics: Insights from first principles. *Phys. Rev. B* **2014**, *89*, 125203.
- (16) Filippetti, A.; Delugas, P.; Mattoni, A. Radiative recombination and photoconversion of methylammonium lead iodide perovskite by first principles: properties of an inorganic semiconductor within a hybrid body. *J. Phys. Chem. C* **2014**, *118*, 24843–24853.
- (17) Pisoni, A.; Jaćimović, J.; Barišić, O. S.; Spina, M.; Gaál, R.; Forró, L.; Horváth, E. Ultra-low thermal conductivity in organic-inorganic hybrid perovskite $\text{CH}_3\text{NH}_3\text{PbI}_3$. *J. Phys. Chem. Lett.* **2014**, 2488–2492.
- (18) Wehrenfennig, C.; Liu, M.; Snaith, H. J.; Johnston, M. B.; Herz, L. M. Homogeneous emission line broadening in the organo lead halide perovskite $\text{CH}_3\text{NH}_3\text{PbI}_3$. *J. Phys. Chem. Lett.* **2014**, *5*, 1300–1306.
- (19) Liu, J.; Prezhdov, O. V. Chlorine doping reduces electron-hole recombination in lead. *J. Phys. Chem. Lett.* **2015**, *6*, 4463–4469.
- (20) Delugas, P.; Filippetti, A.; Mattoni, A. Methylammonium fragmentation in amines as source of localized trap levels and the healing role of Cl in hybrid lead-iodide perovskites. *Phys. Rev. B* **2015**, *92*, 045301.
- (21) Frost, J. M.; Butler, K. T.; Walsh, A. Molecular ferroelectric contributions to anomalous hysteresis in hybrid perovskite solar cells. *APL Mater.* **2014**, *2*, 081506.
- (22) Filippetti, A.; Delugas, P.; Saba, I.; Mattoni, A. Entropy-suppressed ferroelectricity in hybrid lead-iodide perovskites. *J. Phys. Chem. Lett.* **2015**, *6*, 4909–4915.
- (23) Wasylishen, R.; Knop, O.; Macdonald, J. Cation rotation in methylammonium lead halides. *Solid State Commun.* **1985**, *56*, 581–582.

- (24) Leguy, A. M. a.; Frost, J. M.; McMahon, A. P.; Sakai, V. G.; Kochelmann, W.; Law, C.; Li, X.; Foglia, F.; Walsh, A.; O'Regan, B. C. et al. The dynamics of methylammonium ions in hybrid organic-inorganic perovskite solar cells. *Nat. Commun.* **2015**, *6*, 7124.
- (25) Chen, T.; Foley, B. J.; Ipek, B.; Tyagi, M.; Copley, J. R. D.; Brown, C. M.; Choi, J. J.; Lee, S. H. *Phys. Chem. Chem. Phys.* **2015**, *17*, 31278–31286.
- (26) Carignano, M. A.; Kachmar, A.; Hutter, J. Thermal effects on $\text{CH}_3\text{NH}_3\text{PbI}_3$ perovskite from ab initio molecular dynamics simulations. *J. Phys. Chem. C* **2015**, *119*, 8991–8997.
- (27) Goehry, C.; Nemnes, G. A.; Manolescu, A. Collective behavior of molecular dipoles in $\text{CH}_3\text{NH}_3\text{PbI}_3$. *J. Phys. Chem. C* **2015**, *119*, 19674–19680.
- (28) Mattoni, A.; Filippetti, A.; Saba, M. I.; Delugas, P. Methylammonium rotational dynamics in lead halide perovskite by classical molecular dynamics: the role of temperature. *J. Phys. Chem. C* **2015**, *119*, 17421–17428.
- (29) Onoda-Yamamuro, N.; Matsuo, T.; Suga, H. Calorimetric and IR spectroscopic studies of phase transitions in methylammonium trihalogenoplumbates (II). *J. Phys. Chem. Solids* **1990**, *51*, 1383–1395.
- (30) Mosconi, E.; Quarti, C.; Ivanovska, T.; Ruani, G.; De Angelis, F. Structural and electronic properties of organo-halide lead perovskites: a combined IR-spectroscopy and ab initio molecular dynamics investigation. *Phys. Chem. Chem. Phys.* **2014**, *16*, 16137–44.
- (31) Glaser, T.; Müller, C.; Sendner, M.; Krekeler, C.; Semonin, O. E.; Hull, T. D.; Yaffe, O.; Owen, J. S.; Kowalsky, W.; Pucci, A. et al. Infrared spectroscopic study of vibrational modes in methylammonium lead halide perovskites. *J. Phys. Chem. Lett.* **2015**, 2913–2918.

- (32) Quarti, C.; Grancini, G.; Mosconi, E.; Bruno, P.; Ball, J. M.; Lee, M. M.; Snaith, H. J.; Petrozza, A.; Angelis, F. D. The raman spectrum of the $\text{CH}_3\text{NH}_3\text{PbI}_3$ hybrid perovskite: interplay of theory and experiment. *J. Phys. Chem. Lett.* **2014**, *5*, 279–284.
- (33) Ledinský, M.; Löper, P.; Niesen, B.; Holovský, J.; Moon, S.-J.; Yum, J.-H.; De Wolf, S.; Fejfar, A.; Ballif, C. Raman spectroscopy of organic-inorganic halide perovskites. *J. Phys. Chem. Lett.* **2015**, *6*, 401–406.
- (34) Brivio, F.; Frost, J. M.; Skelton, J. M.; Jackson, A. J.; Weber, O. J.; Weller, M. T.; Goñi, A. R.; Leguy, A. M. a.; Barnes, P. R. F.; Walsh, A. Lattice dynamics and vibrational spectra of the orthorhombic, tetragonal, and cubic phases of methylammonium lead iodide. *Phys. Rev. B* **2015**, *92*, 144308.
- (35) Pérez-Osorio, M. A.; Milot, R. L.; Filip, M. R.; Patel, J. B.; Herz, L. M.; Johnston, M. B.; Giustino, F. Vibrational properties of the organic-inorganic halide perovskite $\text{CH}_3\text{NH}_3\text{PbI}_3$ from theory and experiment: factor group analysis, first-principles calculations, and low-temperature infrared spectra. *J. Phys. Chem. C* **2015**, *119*, 25703–25718.
- (36) Deretzis, I.; Alberti, a.; Pellegrino, G.; Smecca, E.; Giannazzo, F.; Sakai, N.; Miyasaka, T.; La Magna, a. Atomistic origins of $\text{CH}_3\text{NH}_3\text{PbI}_3$ degradation to PbI_2 in vacuum. *Appl. Phys. Lett.* **2015**, *106*, 131904.
- (37) Giannozzi, P.; Baroni, S.; Bonini, N.; Calandra, M.; Car, R.; Cavazzoni, C.; Ceresoli, D.; Chiarotti, G. L.; Cococcioni, M.; Dabo, I. et al. QUANTUM ESPRESSO: a modular and open-source software project for quantum simulations of materials. *J. Phys. Condens. Matter* **2009**, *21*, 395502.
- (38) Humphrey, W.; Dalke, A.; Schulten, K. VMD: Visual molecular dynamics. *J. Mol. Graph.* **1996**, *14*, 33–38.

- (39) Todorov, I. T.; Smith, W.; Trachenko, K.; Dove, M. T. DL_POLY_3: new dimensions in molecular dynamics simulations via massive parallelism. *J. Mater. Chem.* **2006**, *16*, 1911.
- (40) Saba, M. I.; Mattoni, A. Simulations of oxide/polymer hybrids. *Encycl. Nanotechnol.* **2015**, 1–13.
- (41) Caddeo, C.; Dessí, R.; Melis, C.; Colombo, L.; Mattoni, A. Poly(3-hexylthiophene) adhesion on zinc oxide nanoneedles. *The Journal of Physical Chemistry C* **2011**, *115*, 16833–16837.
- (42) Melis, C.; Raiteri, P.; Colombo, L.; Mattoni, A. Self-Assembling of Zinc Phthalocyanines on ZnO (10 $\bar{1}$ 0) Surface through Multiple Time Scales. *ACS Nano* **2011**, *5*, 9639–9647.
- (43) Mattioli, G.; Melis, C.; Mallocci, G.; Filippone, F.; Alippi, P.; Giannozzi, P.; Mattoni, A.; Amore Bonapasta, A. Zinc oxide – zinc phthalocyanine interface for hybrid solar cells. *The Journal of Physical Chemistry C* **2012**, *116*, 15439–15448.
- (44) La-o-vorakiat, C.; Kadro, J. M.; Salim, T.; Zhao, D.; Ahmed, T.; Lam, Y. M.; Zhu, J.-X.; Marcus, R. a.; Michel-Beyerle, M.-E.; Chia, E. E. Phonon mode transformation across the orthorhombic-tetragonal phase transition in a lead-iodide perovskite CH₃NH₃PbI₃ : a Terahertz time-domain spectroscopy approach. *J. Phys. Chem. Lett.* **2015**, acs.jpcllett.5b02223.

Supporting Information of "Temperature Evolution of Methylammonium Trihalide Vibrations at the Atomic Scale"

A. Mattoni,* A. Filippetti, M.I. Saba, C. Caddeo, and P. Delugas

Istituto Officina dei Materiali, CNR-IOM SLACS Cagliari, 09042 Monserrato (CA)

E-mail: mattoni@iom.cnr.it

Static calculation of phonons

- The vibrational properties of the isolated MA cation (+1 charge state) are obtained by the diagonalization of the dynamical matrix $D_{ij} = M_i^{-\frac{1}{2}} \frac{dF_i}{dx_j} M_j^{-\frac{1}{2}}$, obtained through finite difference method ($\frac{dF_i}{dx_j} = \frac{1}{2\delta_j} F_i(x + \delta_j) - F_i(x - \delta_j)$). The calculations have been performed by using a in-house developed code that can be interfaced with both QUANTUM ESPRESSO¹ and DL_POLY 4.0.2 code.²
- For periodic crystals, the Fourier transform of the dynamical matrix

$$D_{bb'}^k = \frac{1}{N_c} \sum_l M_i^{-\frac{1}{2}} \frac{dF_b^l}{dx_{b'}^0} M_j^{-\frac{1}{2}} e^{ik(R_0 - R_l)}$$

is required, where b, b' label the atoms of the unit cell and R_l the Bravais vector of the l -th replica, (l running over N_c units forming the system). For the orthorhombic MAPI crystal a good approximation is $|l| \leq 2$. This is shown in the second row of Figure S1 reporting the phonon dispersion of MAPI crystal (orthorhombic P0) calculated as a function of the number of replicas along the cartesian directions (in the range 1x1x1 up to 4x4x4 unit cells). The result does not change sizably for systems larger than 2x2x2. Accordingly the 2x2x2 MAPI crystal ($48 \times 8 = 384$ atoms) is used for the DFT calculation of the dynamical matrix. The computational workload is high (about 50000 CPU hours) but consisting of 144x6 independent self-consistent calculations (embarassingly parallel). Previous works made use of single cell calculations at Γ point by perturbation theory methods.^{3,4}

- The molecular character of a mode $\nu(k)$ (k in the first B.Z. of the lattice) of atomic components $c_\nu^i(k)$ ($i = 1, 3N$) is defined as $\chi_{\nu(k)} = \sum_{i \in M} |c_\nu^i(k)|^2$ where i runs over the subset M of atoms forming the molecules. If the mode is normalized then $0 \leq \chi_{\nu(k)} \leq 1$.

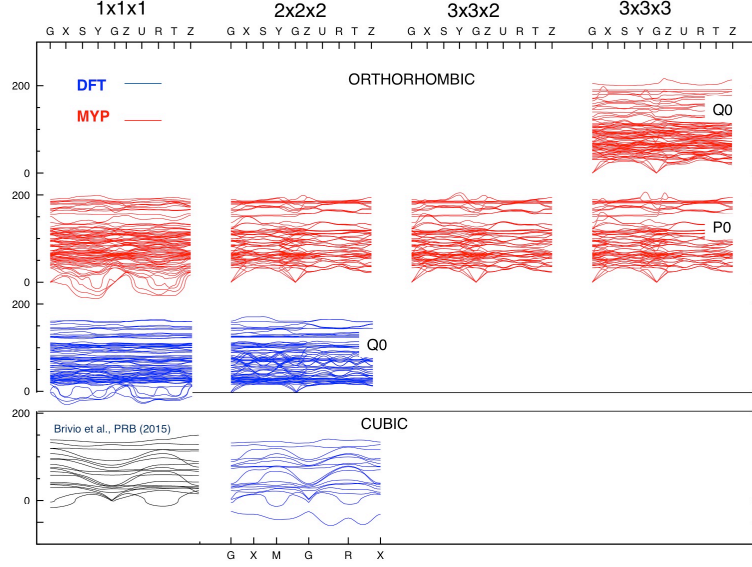


Figure S1: Phonon dispersion curves calculated by DFT (blue) and MYP (red) by using different number of replica in the dynamical matrix calculation and considering orthorhombic (P0, Q0) and cubic crystals. The result of Brivio et al.³ is reported for comparison.

Atomic forces calculations

- First principles interatomic forces necessary to calculate the dynamical matrix have been calculated by using the QUANTUM ESPRESSO¹ package. Planewaves basis sets have been used with kinetic energy cutoff equal to 35 rydberg and 250 rydberg for wavefunctions and density, respectively. The Brillouin zone was sampled by a 4x4x4 Monkhorst-Pack grid. The atomic positions are optimized with force convergence threshold as small as 10^{-4} rydberg/bohr = 0.0025 eV/angstrom.
- Different orthorhombic configurations have been considered in this work (labeled as P0, Q0, Q0') in order to calculate of the vibrational density of states and phonon dispersion.

The P0 configuration is available as supporting material of the work by Filippetti et al.⁵ and it corresponds to one of the quasi-isoenergetic molecular configurations of the orthorhombic crystal;

the Q0 structure was obtained by starting from the P0 configuration followed by suitable C-N switching to compensate molecular dipoles according to a Pnma-like configuration.

Finally, the orthorhombic Q0' configuration (that is discussed below when comparing DFT and MYP) was obtained by a further volume relaxation and a triclinic metric tensor optimization. In the DFT calculations, the experimental values of lattice parameters (a=8.8362, b=8.555 and c=12.5804) were used for the P0 and Q0 configurations. As for the MYP calculations the Q0 corresponds to the minimum energy configuration obtained after a long annealing at 50 K and relaxed to zero temperature (both atomic positions and metric tensor). The P0 configuration is obtained from the DFT-relaxed P0 structure, followed by a T=0 K local relaxation by the MYP interatomic forces.

Finite temperature dynamical calculations

- Finite temperature MD calculations have been performed by the DL_POLY code² with the same computational setup and model potential parameters described in Ref 6. Simulation cells contained 4x4x4 orthorhombic crystals with 3072 atoms and were annealed for at least 0.3 ns.
- The vibrational densities of states at finite temperature have been obtained by the mass weighted velocity auto-correlation function $vac(t) = \int dt' \sum_{i=1,3N} m_i v_i(t') v_i(t'+t)$ upon Fourier transformation $\rho(\omega) = \frac{1}{t_s} \int_0^{t_s} dt vac(t) / vac(0) e^{-i\omega t}$ (t_s is the simulation time). Projections were obtained by summing over the corresponding subgroups of atoms (MA,PI,C,H,N) in the calculation of the $vac(t)$ auto-correlation function.
- The vibrational modes have been obtained by Fourier transforming the mass-weighted velocities $u_i(\omega) = \int dt m_i^{\frac{1}{2}} v_i(t) e^{-i\omega t}$ and represented by arrows on the atoms of reference equilibrium configuration. Among the 256 molecules of the simulated crystals, the most relevant modes were selected by visual inspection. An example is reported in

Figure S2 where the $\sim 145 \text{ cm}^{-1}$ modes of a subset of eight molecules are represented at two different temperatures. Energy and volume fluctuations at finite temperature make it possible the mixing of zero temperature normal modes.

- Infrared spectra $ir(\omega)$ were obtained by Fourier transforming the current autocorrelation function $jac(t) = \int dt' \sum_{i=1,3N} q_i v_i(t') q_i v_i(t' + t)$ with the fixed atomic charges q_i of the MYP potential. For a better comparison with the experiments it is necessary to reduce the polarity of the ammonium group (while keeping the total molecular charge at the value 1.36). In the present analysis it were used $q_H = 0.34$ and $q_N = -0.5$ instead of the original MYP values 0.54 and -1.1 , respectively. The other charges can be found in Ref. 6. All charges are expressed in units of electronic charge.

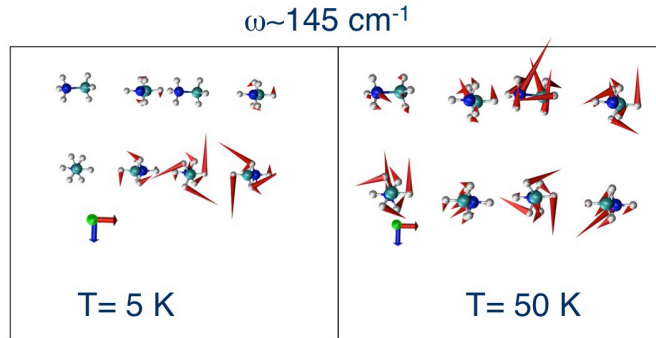


Figure S2: Examples of MA spectral modes calculated during the dynamics at T=5 K and T=50 K

Vibrational spectrum of isolated MA cation by DFT

In this section we report the extensive DFT analysis of the methylammonium. The vibrational spectrum of the MA cation in +1 charge state is reported in Figure S3. The 24 vibrational degrees of freedom of the methylammonium (MA) molecule (8 atoms, 3 cartesian coordinates) give 18 normal modes with frequencies in the range 292 cm^{-1} - 3374 cm^{-1} ,

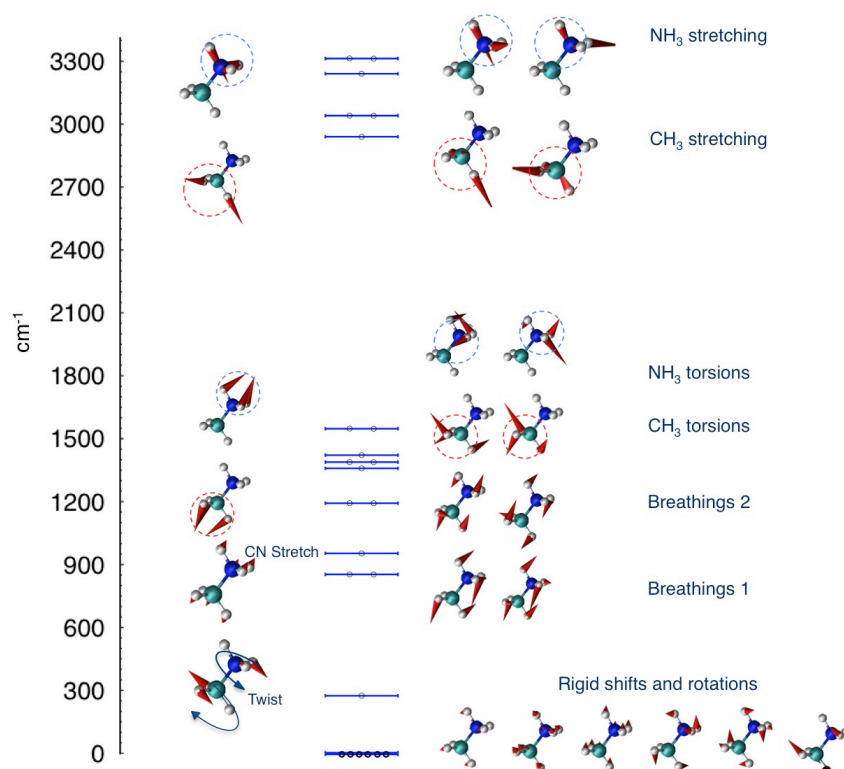


Figure S3: Methylammonium normal frequencies (divided by speed of light ν/c) and mass weighted modes (red arrows in the sticks&balls representation) calculated by DFT.

and six zero energy modes (rigid shifts and rotations, including the spinning around the CN axis). The DFT calculated frequencies (see Figure S3) are in agreement with data reported in literature.^{3,7,8} Only singlets or doubly degenerate modes are possible (see circles in Figure S3) consistent with the representations A_1 , A_2 , or E of the C_{3v} symmetry group of the molecule, respectively.⁹ The lowest non-zero frequency mode of the molecule at 290 cm⁻¹ is the A_2 twisting around C-N axis (with CH_3 and NH_3 rotating in opposite direction); two breathings (E) are found at 879 cm⁻¹; the CN stretching mode (A_1) is at 980 cm⁻¹. The modes at higher frequencies (A_1 singlets and E doublets) correspond to more localized modes with highest ones associated to the distortions and stretching of the stiffer NH_3 group.

Vibrational spectrum of cubic-MAPI crystals by DFT and cubic-to-orthorhombic instabilities

A comparison between the cubic and orthorhombic phonon dispersion curves is reported in Figure S4. The cubic phase is not the fundamental crystal structure at low temperature and it is simulated by imposing the cubic symmetry during the calculations. By performing molecular dynamics simulations of a large cubic crystal at low temperature it is found that the PI octahedra spontaneously give rise to distortions and the system undergoes a transition to the orthorhombic phase. This is the explanation of the negative frequencies observed at M and R point of the reciprocal space in the cubic phonon dispersion. Negative frequencies correspond to directions of structural instabilities (the configuration is not a minimum but a saddle point of the configurational energy). The corresponding atomic displacements are reported in the insets (panel b), clearly showing octahedra rotations in the directions perpendicular to the corresponding reciprocal vector (k_M or k_R). For example, at the reciprocal point $M=(0.5,0.5,0)$ (in units of $\frac{2\pi}{a_i}$, $i = 1, 2, 3$) the imaginary mode is an infinitesimal rotation orthogonal to the $\langle 1,1,0 \rangle$ direction (see small arrows on I atoms). Being k_M at the Brillouin boundary a phase factor $e^{i\pi m}$ appears (m integer number counting the cell of the lattice). The mode consists of rotations with opposite signs that drive the system from

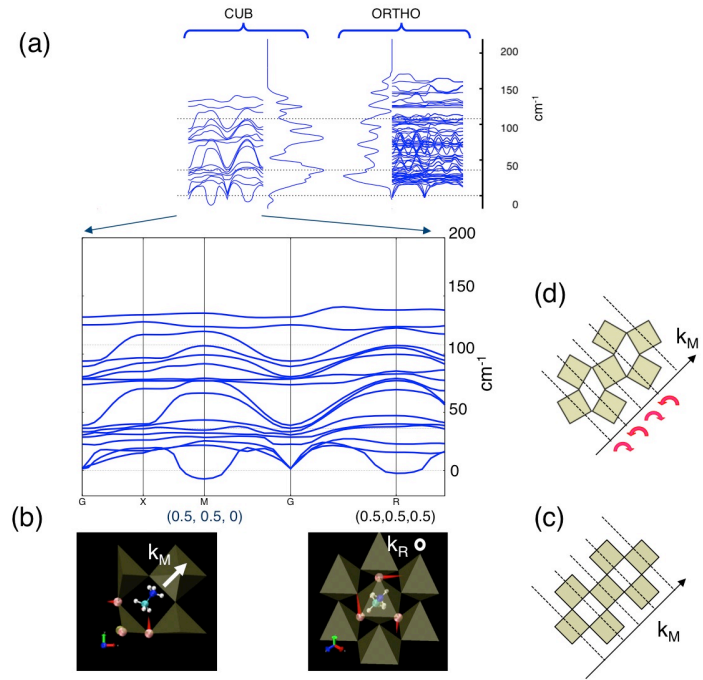


Figure S4: Vibrational dispersion curves for the cubic phase showing negative frequencies at R and M points for both MD and DFT. The corresponding modes are instabilities associated to octahedra rotations of the cubic-orthorhombic phase transformation.

the cubic (c scheme) to the orthorhombic (d scheme) phase. Similar analysis is possible for the R point, along the $\langle 1,1,1 \rangle$ direction. Notably, the imaginary modes and the structural instabilities are not found in the phonon dispersion of the orthorhombic phase, demonstrating that the orthorhombic phase is a proper minimum of the configurational energy of the material.

Classical model potential (MYP) versus ab initio DFT calculations

- The comparison between the vibrational spectrum of isolated MA cation calculated by DFT and MYP potential is reported in Figure S5. It is found an overall qualitative agreement for what concerns the energy order and the type and symmetry of the normal modes. The energy ordering of CN stretching mode and B₂ doublet is exchanged in DFT and MYP. The largest differences between MYP and DFT are found for the CH₃ and NH₃ stretching modes at high frequencies that are overestimated in the MYP case. The agreement is acceptable considering the simplicity of the classical force field^{6,10} that does not include polarizability effects.
- The comparison between the spectrum of the isolated MA and the MAPI crystal (cubic and orthorhombic) is reported in Figure S6, where both DFT (blue) and MYP (red) results are reported. The zero frequency roto-translations of the free MA are raised in the MAPI crystal, giving rise to a band at 100-200 cm⁻¹ represented by the dashed regions in the VDOS.
- The MAPI spectrum and in particular the molecular 70-200 cm⁻¹ band are dependent on the actual structure and molecular configurations. For example, in column b we report the case of cubic MAPI crystal, with its phonon dispersion (panel a) in good agreement with previous results based on DFT perturbation theory.³ The width of the molecular band in the cubic MAPI (dashed region) is sizably reduced because of the

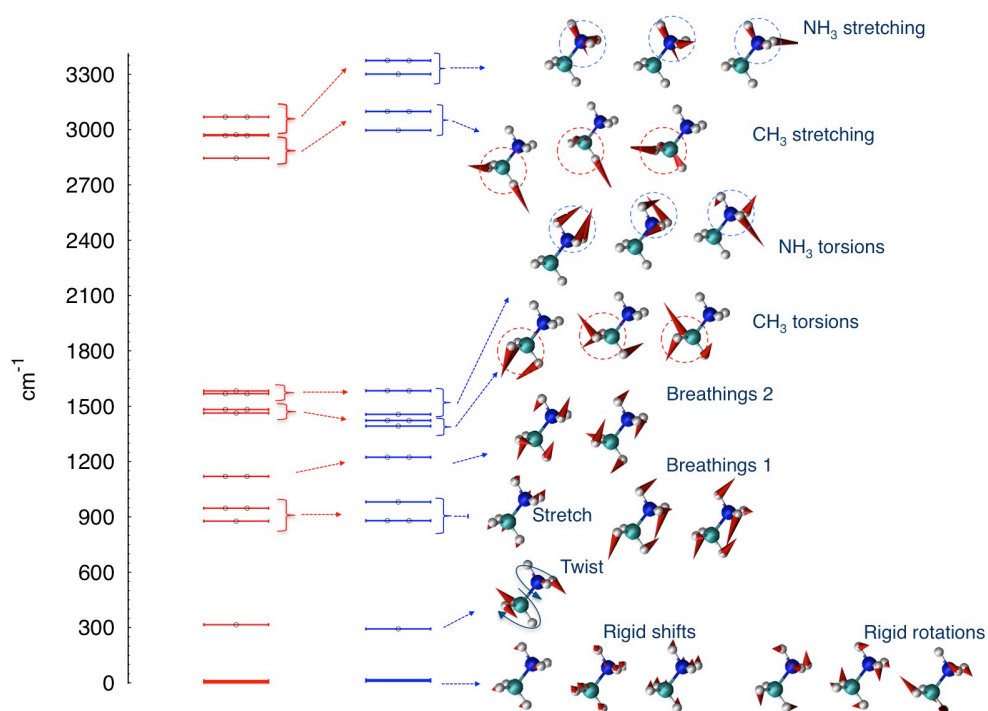


Figure S5: Vibrational spectrum of isolated MA cation (+1 charge) calculated by MYP (left) and DFT (right). Corresponding energy levels are connected by arrows.

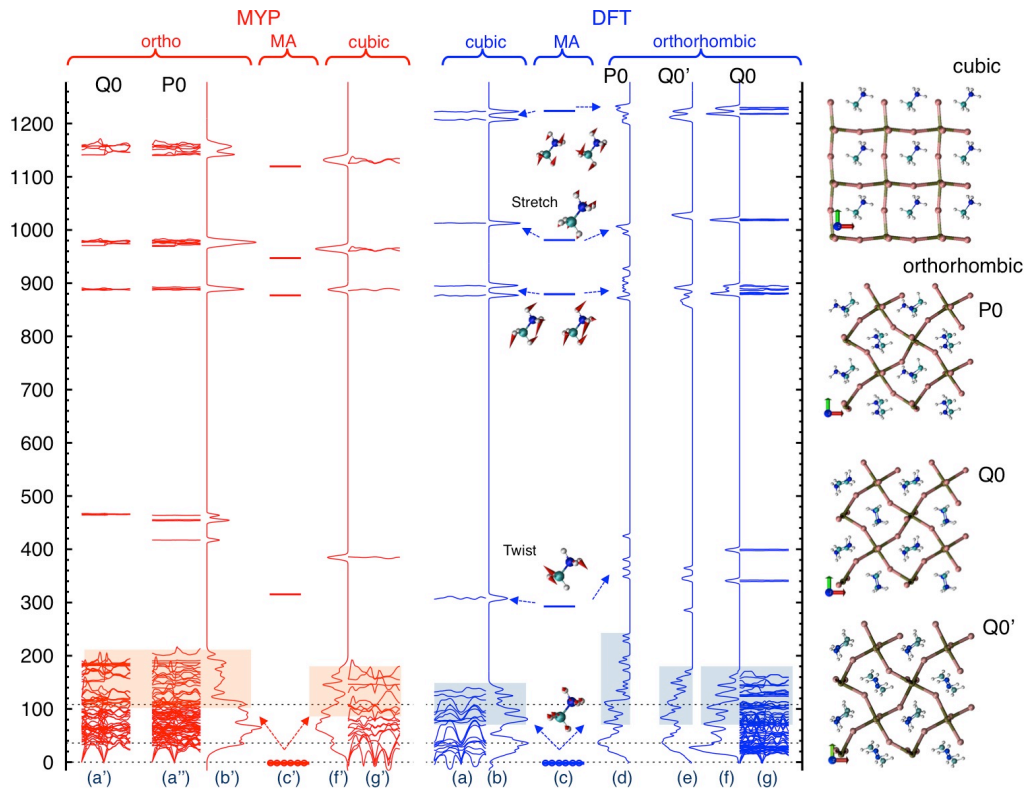


Figure S6: Vibrational density of states and phonon dispersion of MA and MAPI (cubic and orthorhombic crystals) calculated by MYP (red) and DFT (blue). The different orthorhombic crystals (Q0, P0, and Q0') are reported in the right panel.

higher symmetry of the molecular distribution. Furthermore, a molecular level close to the twisting of the isolated MA cation appears. This latter is explained as a reduction of the molecular confinement.

- Concerning the effect of the molecular pattern we have further calculated the VDOS and the vibrational dispersion of P0 orthorhombic structure (panels d and b') for comparison with Q0 one (compare d and f for DFT and a' a'' for MYP)..
- The results calculated on different orthorhombic structures (P0 and Q0) shows the same qualitative VDOS but sizable differences in the detailed positions of the peaks (see d and f for DFT and a' and a'' for MYP). We conclude that the result at T=0 K are an important reference but they are not fully representative of the system even at low temperature where several minima are explored. Also the impact of the DFT computational details⁴ are a minor effect with respect to the structure and to the molecular ordering. A more accurate comparison between MYP and DFT is given in Figure S7.
- The vibrational peaks at T=0K of the DFT vibrational density of states (in cm⁻¹) are: R at 160, 164, 170; S at 145.5; R_N at 126; T at 102, R_C at 72.9; T_w 399, 341; B₁ at 881, S_t at 1018; B₂ at 1220, 1357, 1401

Orthorhombic-MAPI phonons: DFT versus rescaled MYP

The model potential has been fit on properties different from vibrational modes⁶ and so the accuracy of the model can only be checked a posteriori by comparing ab initio and MYP results. The MYP potential reproduces the same vibrational structure of ab initio but it tends to blueshift the crystal frequencies by about 30% indicating stiffer interactions K ($K/M \propto \omega^2$). The rescaling is a practical way to extract more quantitative results from the classical model. The fact that the rescaling factor is larger than one means that the classical model tends to overestimate the energy cost

during ionic displacement and this can be explained by the use of fixed charge models in which the charge cannot redistribute so giving a smaller polarizability. In order to get a more quantitative prediction it would be necessary to refine the MYP potential (by a refitting procedure that includes the dispersion curves, possibly making use of more complex functional forms such as bond order or shell models). This is beyond the limit of the present investigation. Here, we identify as practical solution for a better quantitative comparison with DFT to rescale the MYP spectrum below 600 cm^{-1} by a factor 1.27 that gives the best agreement between MYP and DFT (see Figure S7).

The MYP spectra have similar peaks to the DFT: S at 145.5 ; R_N at 126 ; T at 102 . The R_N peak is smaller in the Q0 structure. In the MYP cases the R_N peak is broadened, particularly in the Q0 structure; furthermore the R_C region is characterized by a larger PI contribution.

The additional peaks in the VDOS at finite temperature are: R 170 , X 250 , $T_w \sim 330, 360$, S_t 890 , B_1 975 , B_2 $1140-1160\text{ cm}^{-1}$

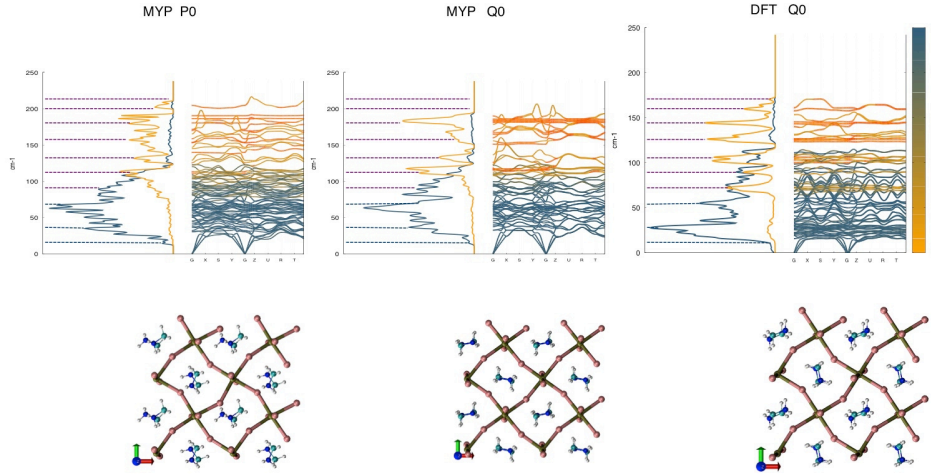


Figure S7: Phonon dispersion of the orthorhombic MAPI crystal (Q0) calculated by DFT (right panel) and by MYP classical potential (middle panel); a crystal structure with an alternative molecular pattern, P0, is reported in left panel for comparison. Upon shrinking the vibrational frequencies by 27%, a qualitative correspondence between DFT and MYP is found.

Cubic-, tetragonal- and orthorhombic-MAPI phonons by MYP: static versus dynamic results

In the right panels of Figure S8 we report the phonon dispersion curves of the cubic, tetragonal and orthorhombic-MAPI crystals calculated by the MYP potential. We focus here on the Q0 configuration (with anti-aligned molecules). The low vibrational bands have been rescaled as discussed in the previous sections. For the tetragonal phase we used the I0 configuration at the experimental lattice parameters described in a previous work.¹¹ By moving from the Ortho- to cubic- phase we can observe a progressive lowering of the bands and imaginary frequencies are found associated to favorable internal and cell distortions. We stress that the cubic and tetragonal phases are properly stable only at finite temperature. In fact they are minima of the free energy (not necessarily of the internal energy) and represent the thermodynamic average over a large set of instantaneous configurations of lower symmetry. The molecular levels tend to red-shift as a result of the volume expansion and the reduced hybrid interactions. In other words the actual position of the molecular level is very sensitive to the local relaxation and it can be properly described only dynamically. This is very clear by comparing the static and dynamic VDOS. By comparing the corresponding crystal structure we conclude that there are sizable differences in the position of the peaks, for example the R one. Furthermore the height and width of the peaks provide information about the phonon lifetime and anharmonic effects.

Comparison with experimental data

In Figure S9 we report in more detail (with respect to the main text) the IR calculated spectra at T=10 K (bottom), T=50 K (middle) and T=300 K (top) and compare the evolution of the main peak at 50-60 cm^{-1} with the results on vibrational properties based on Terahertz Time-Domain Spectroscopy¹² at T= 20 K (bottom) and T=300 K (top).

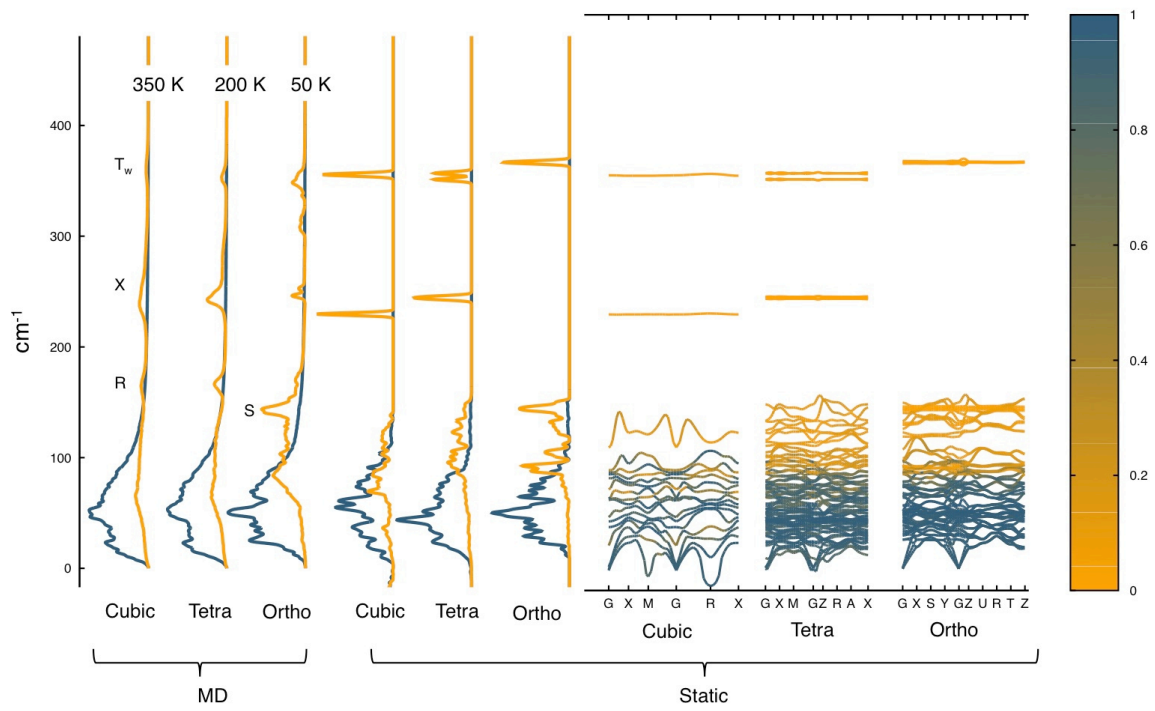


Figure S8: Comparison between static (right) and dynamic (left) vibrational analysis of the cubic, tetragonal and orthorhombic MAPI phonons (right) and vibrational density of states (left). A color palette is used: orange (steel-blue) for organic (inorganic) character.

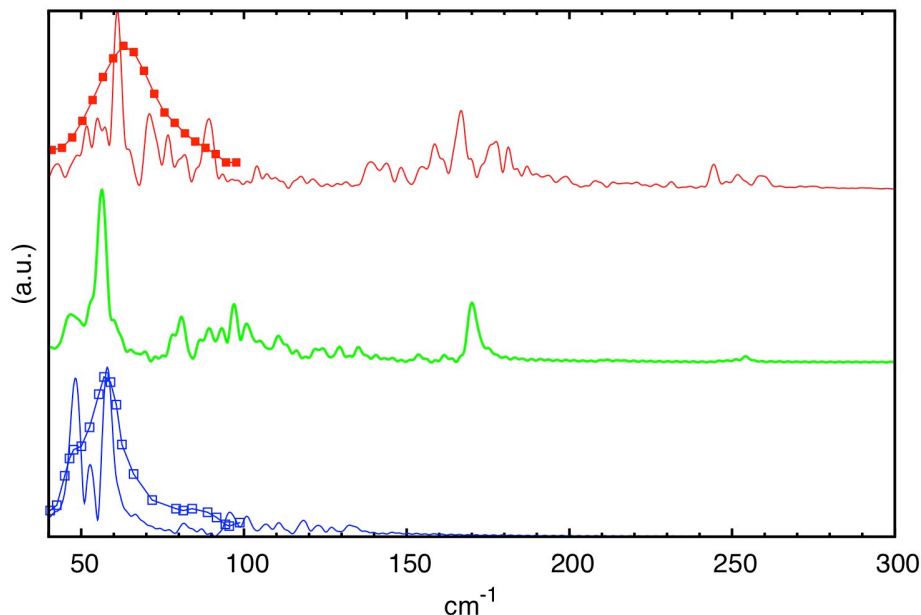


Figure S9: Comparison with experimental data.

References

- (1) Giannozzi, P.; Baroni, S.; Bonini, N.; Calandra, M.; Car, R.; Cavazzoni, C.; Ceresoli, D.; Chiarotti, G. L.; Cococcioni, M.; Dabo, I. et al. QUANTUM ESPRESSO: a modular and open-source software project for quantum simulations of materials. *J. Phys. Condens. Matter* **2009**, *21*, 395502.
- (2) Todorov, I. T.; Smith, W.; Trachenko, K.; Dove, M. T. DL_POLY_3: new dimensions in molecular dynamics simulations via massive parallelism. *J. Mater. Chem.* **2006**, *16*, 1911.
- (3) Brivio, F.; Frost, J. M.; Skelton, J. M.; Jackson, A. J.; Weber, O. J.; Weller, M. T.; Goñi, A. R.; Leguy, A. M. a.; Barnes, P. R. F.; Walsh, A. Lattice dynamics and vibrational spectra of the orthorhombic, tetragonal, and cubic phases of methylammonium lead iodide. *Phys. Rev. B* **2015**, *92*, 144308.

- (4) Pérez-Osorio, M. A.; Milot, R. L.; Filip, M. R.; Patel, J. B.; Herz, L. M.; Johnston, M. B.; Giustino, F. Vibrational properties of the organic-inorganic halide perovskite $\text{CH}_3\text{NH}_3\text{PbI}_3$ from theory and experiment: factor group analysis, first-principles calculations, and low-temperature infrared spectra. *J. Phys. Chem. C* **2015**, *119*, 25703–25718.
- (5) Filippetti, A.; Delugas, P.; Mattoni, A. Radiative recombination and photoconversion of methylammonium lead iodide perovskite by first principles: properties of an inorganic semiconductor within a hybrid body. *J. Phys. Chem. C* **2014**, *118*, 24843–24853.
- (6) Mattoni, A.; Filippetti, A.; Saba, M. I.; Delugas, P. Methylammonium rotational dynamics in lead halide perovskite by classical molecular dynamics: the role of temperature. *J. Phys. Chem. C* **2015**, *119*, 17421–17428.
- (7) Quarti, C.; Grancini, G.; Mosconi, E.; Bruno, P.; Ball, J. M.; Lee, M. M.; Snaith, H. J.; Petrozza, A.; Angelis, F. D. The raman spectrum of the $\text{CH}_3\text{NH}_3\text{PbI}_3$ hybrid perovskite: interplay of theory and experiment. *J. Phys. Chem. Lett.* **2014**, *5*, 279–284.
- (8) Mosconi, E.; Quarti, C.; Ivanovska, T.; Ruani, G.; De Angelis, F. Structural and electronic properties of organo-halide lead perovskites: a combined IR-spectroscopy and ab initio molecular dynamics investigation. *Phys. Chem. Chem. Phys.* **2014**, *16*, 16137–44.
- (9) Boris S. Tsukerblat, *Group theory in chemistry and spectroscopy. A simple guide to advanced usage.*; Academic Press, London: London, 1994; p 464.
- (10) Ponder, J. W.; Case, D. A. Force fields for protein simulations. *Adv. Prot. Chem.* **2003**, *66*, 27–85.
- (11) Filippetti, A.; Mattoni, A. Hybrid perovskites for photovoltaics: Insights from first principles. *Phys. Rev. B* **2014**, *89*, 125203.

- (12) La-o-vorakiat, C.; Kadro, J. M.; Salim, T.; Zhao, D.; Ahmed, T.; Lam, Y. M.; Zhu, J.-X.; Marcus, R. a.; Michel-Beyerle, M.-E.; Chia, E. E. Phonon mode transformation across the orthorhombic-tetragonal phase transition in a lead-iodide perovskite $\text{CH}_3\text{NH}_3\text{PbI}_3$: a Terahertz time-domain spectroscopy approach. *J. Phys. Chem. Lett.* **2015**, acs.jpcllett.5b02223.